PERFORMANCE AND ROBUSTNESS OF A MULTISTATIC MIST BEAMFORMING ALGORITHM FOR BREAST CANCER DETECTION

M. O'Halloran, M. Glavin, and E. Jones [†]

College of Engineering and Informatics
National University of Ireland Galway
University Road, Galway, Ireland

Abstract—Ultra-Wideband (UWB) radar is one of the most promising emerging technologies for the early detection of breast cancer, and the development of robust beamforming algorithms for imaging has been the subject of a significant amount of research. Extending the monostatic Microwave Imaging via Space Time (MIST) beamformer originally developed by Bond et al., the authors proposed the Multistatic MIST beamforming algorithm that uses the spatial diversity of the receiving antennas to acquire more energy reflected from dielectric scatterers which propagate outwards via different routes, while compensating for multistatic path-dependent attenuation and phase effects. In this paper, the performance and robustness of the Multistatic MIST beamformer is examined across a range of potential clinical scenarios. The multistatic beamformer is directly compared with the traditional monostatic beamformer and the effects of the additional multistatic channels is investigated. Furthermore, the robustness of the beamformer with respect to tumor size and location, variations in dielectric properties, and significantly, different fibroglandular tissue distributions within the breast based on recently published data, is examined.

Corresponding author: M. O'Halloran (martin.ohalloran@gmail.com).

[†] M. Glavin and E. Jones are also with Bioelectronics Research Cluster, National Centre for Biomedical Engineering Science (NCBES), National University of Ireland Galway, University Road, Galway, Ireland. M. O'Halloran is also with Bioelectronics Research Cluster, National Centre for Biomedical Engineering Science (NCBES), National University of Ireland Galway, University Road, Galway, Ireland; and College of Engineering and Informatics, National University of Ireland Galway, University Road, Galway, Ireland.

1. INTRODUCTION

Breast cancer is one of the most common cancers in women. In the United States alone, it accounts for 31% of new cancer cases, and is second only to lung cancer as the leading cause of deaths in American women [1]. More than 184,000 new cases of breast cancer are diagnosed each year resulting in approximately 41,000 deaths [1]. However, breast cancer mortality is on the decline in industrialized countries like as the United States, Canada, Germany, Austria and the United Kingdom [2]. This decline can be attributed in no small part to increased breast cancer screening, and the early detection and treatment of the disease. Earlier detection and intervention is one of the most significant factors in improving the survival rates and quality of life experienced by breast cancer sufferers [2], since this is the stage when treatment is most effective. While X-ray mammography is currently the standard imaging modality for detecting early-stage non-palpable breast cancer, it's inherent limitations in terms of sensitivity and specificity are well documented [2].

One of the most promising breast imaging modalities is microwave imaging. Two alternative active microwave imaging techniques are currently under development, Microwave Tomography and Ultra-Wideband (UWB) Radar imaging. Microwave Tomography involves reconstructing the complete dielectric profile of the breast using a forward and inverse scattering model [3–7]. The tomographic approach has shown significant promise in both detecting small tumors [8, 9] and also differentiating between malignant and benign tissue for lesions as small as 1 cm in diameter [9].

On the other hand, Ultra-Wideband (UWB) Radar imaging, as proposed by Hagness et al. [10], uses reflected UWB signals to determine the location of microwave scatterers within the breast. Rather than using the tomographic approach of reconstructing the entire dielectric profile of the breast, UWB radar imaging uses the Confocal Microwave Imaging (CMI) approach [10] to identify and locate regions of scatterings within the breast [11–19]. Adaptive beamforming is typically used to process the backscattered signals, and to compensate for frequency-dependent propagation effects [20–26].

In a monostatic beamformer, each antenna in turn illuminates the breast and the reflected energy is recorded only at the transmitting antenna. In some monostatic approaches, the transmitting antenna is moved across the breast to produce a synthetic aperture. Conversely, in the multistatic approach, the tissue is illuminated by one transmitting antenna while the backscattered signals are recorded at several antennas placed at different positions around the breast. As described

by Xie et al. [24], the multistatic approach can produce better imaging results when the actual aperture used in the multistatic system is close to the synthetic aperture used in the monostatic case. A multistatic imaging system has been developed by Craddock et al. [27, 28], while several other multistatic imaging algorithms have been developed and demonstrated, including a simple Delay and Sum (DAS) [29] and a Robust Capon Beamforming (RCB)-based adaptive method [24, 25, 30]. Bond et al. proposed a monostatic MIST beamformer which is described in [20]. The Multistatic MIST beamformer [31] examined here extends the monostatic MIST beamformer algorithm, compensating for attenuation and phase effects as the multistatic signals propagate through the breast. The multistatic MIST beamformer has been previously shown to significantly outperform the monostatic MIST beamformer from which it is derived [31].

A recent study of the dielectric properties of adipose, fibroglandular and cancerous breast tissue has highlighted the dielectric heterogeneity of normal breast tissue [32, 33]. The dielectric properties of adipose tissue were found to be lower than any previously published data for normal tissue. Conversely, the dielectric properties of fibroglandular tissue were found to be significantly higher than any previously published data for normal breast tissue. This heterogeneity of normal breast tissue had been considerably underestimated by previous studies [34], and presents a much difficult imaging scenario. Therefore, in order to accurately determine the effectiveness, and indeed limitations of the Multistatic MIST beamformer [31], the ability of the beamformer to accurately identify the presence and location of cancerous tissue within the dielectrically heterogeneous breast is assessed in this paper.

The remainder of the paper is organized as follows: Section 2 describes Multistatic MIST beamforming algorithm; Section 3 describes the test procedure applied to the Multistatic MIST beamformer and the corresponding results; Finally, the conclusions and suggestion for possible future work are discussed in Section 4.

2. MULTISTATIC MIST BEAMFORMER

Consider a planar array of antennas placed across a naturally flattened breast. Each antenna element of the array sequentially transmits a UWB pulse into the breast, and the returns are recorded on all antennas in the array, including the transmitting antenna. For the purposes of this section, it is assumed that the early-stage artifact in each channel has been effectively removed and all that remains is
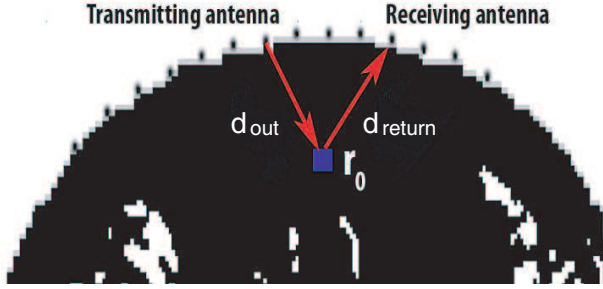
Figure 1. The propagation path distance for multistatic signals is equal to the sum of the outward distance d_{out} and return distance d_{return}. The antennas are shown as black dots located across the surface of the breast. The voxel of interest, r_0, is shown in blue, and the propagation paths d_{out} and d_{return} are shown as red arrows for clarity.

the response from any tumor present and clutter due to the natural heterogeneity of the breast; artifact removal is considered further in Section 3. The first step in the beamforming is coarse time-alignment. Consider a voxel of interest r_0 within the breast, as shown in Figure 1. For each antenna transmission, the propagation distance between the transmitting antenna, the voxel r_0, and the receiving antenna is calculated. The distance is denoted by $d_{(i,j)}$ where i is the transmitting antenna index and j is the corresponding receiving antenna index. For multistatic signals, the distance $d_{(i,j)}$ is defined as:

$$d_{(i,j)} = d_{out} + d_{return} \tag{1}$$

where d_{out} is the distance between the transmitting antenna and r_0 and d_{return} is the distance between r_0 and the receiving antenna, as shown in Figure 1. For the signal recorded at the transmitting antenna itself (the monostatic signals), the distance is simply:

$$d_{(i,i)} = 2d_{out} \tag{2}$$

The round-trip time (in samples) to r_0, and back to the receiving antenna, is calculated as follows:

$$T_{rt(i,j)} = \frac{d_{(i,j)}}{s} f_s \tag{3}$$

where f_s is the sampling frequency, and s is the average speed of propagation in breast tissue and is defined as follows:

$$s = \frac{c}{\sqrt{\epsilon_r}} \tag{4}$$

where ϵ_r is the relative permittivity of normal breast tissue at the centre frequency of the UWB input signal and c is the speed of light. Each of the signals is then delayed, to coarsely time-align all the responses from the candidate location as a pre-processing step to allow further processing to take place. The delay applied to each channel is defined as:

$$delay_{(i,j)} = \max(T_{rt}) - T_{rt(i,j)} \qquad (5)$$

Once the delay is applied to each channel, and the response from the scan location of interest coarsely aligned, the delay term, $\max(T_{rt})$, is removed, to ignore energy from any interference or clutter present outside the time window of interest.

Once the initial time-alignment has taken place, an FIR filter, based on the monostatic beamformer design of Bond et al. [20], is used to mitigate path-length dispersion and attenuation, interpolate any fractional time delays remaining, and bandpass filter the signal. For each multistatic channel i, the FIR filter of length L can be denoted by $\mathbf{w_i} = \begin{bmatrix} w_{i0}, w_{i1}, \ldots, w_{i(L-1)} \end{bmatrix}^T$. The frequency response of each filter is given by:

$$W_{ij}(\omega) = \sum_{l=0}^{L-1} \omega_{il} e^{-j\omega l T_s} = \mathbf{w}_{ij}^T \mathbf{d}(\omega) \qquad (6)$$

where $\mathbf{d}(\omega) = \begin{bmatrix} 1, e^{-j\omega T_s}, \ldots, e^{-j\omega(L-1)T_s} \end{bmatrix}^T$ and T_s is the sampling interval. Assuming the time-alignment step has been completed, the filter coefficients must satisfy the following equation:

$$\sum_{i=0}^{N} \tilde{S_{ij}}(r_0, \omega) \mathbf{w_{ij}^T} \mathbf{d}(\omega) \approx e^{-j\omega T_s(L-1)/2} \qquad (7)$$

where $S_{ij}(r_0, \omega)$ is a model of the channel which affects the input signal as it propagates from the ith transmitting antenna to the target, and back to the jth receiving antenna, and is defined as follows:

$$S_{ij}(r_0, \omega) = \left[\frac{1}{\sqrt{T_{rt(i,j)}}} e^{-\alpha(\omega)T_{rt(i,j)}} e^{-j\beta(\omega)T_{rt(i,j)}} \right] \qquad (8)$$

where $\alpha(\omega)$ is the frequency-dependent attenuation factor and $\beta(\omega)$ is the frequency-dependant phase constant.

There are two differences between this channel model and the model used by Bond et al. [20]. Firstly, Bond et al. calculated the one-way distance between the transmitting antenna and the target, and then squared the channel model to account for the round-trip propagation. This is not appropriate for multistatic signals where d_{out} and d_{return} are often quite different. Secondly, Bond et al. assumed

that $\alpha(\omega)$ and $\beta(\omega)$ are constant and were evaluated at the spectral peak of the input signal. For a more complete representation of the frequency-dependence of the channel, the variation of $\alpha(\omega)$ and $\beta(\omega)$ with frequency is incorporated into the channel model, used here.

Let N define the total number of multistatic channels used, and the filtering weight vector $\mathbf{w}$ as $\mathbf{w} = [\mathbf{w_1^T}, \mathbf{w_2^T}, \ldots, \mathbf{w_N^T}]^\mathbf{T}$; then Equation (7) becomes:

$$\mathbf{w^T}\mathbf{d}(\mathbf{r_0}, \omega) \approx e^{-j\omega T_s(L-1)/2} \tag{9}$$

and $\mathbf{d}(\mathbf{r_0}, \omega)$ is defined as:

$$\mathbf{d}(r_0, \omega) = \begin{bmatrix} \tilde{S_{11}}(r_0, \omega)\mathbf{d}(\omega) \\ \tilde{S_{12}}(r_0, \omega)\mathbf{d}(\omega) \\ . \\ . \\ \tilde{S_{NN}}(r_0, \omega)\mathbf{d}(\omega) \end{bmatrix} \tag{10}$$

To ensure the filter weights are real-valued, Equation (9) is evaluated across positive and negatives frequencies within the frequency band $[\omega_l, \omega_u]$. The vector $d(r_0, \omega)$ at each of the discrete frequencies across the band is contained within matrix $\mathbf{A}$:

$$\mathbf{A} = [\mathbf{d}(r_0, \omega_1), \ldots, \mathbf{d}(r_0, \omega_M)] \tag{11}$$

and Equation (9) now becomes:

$$\mathbf{w^T}\mathbf{A} \approx f_d \tag{12}$$

where

$$f_d = \left[e^{-j\omega_1 T_s(L-1)/2}, \ldots, e^{-j\omega_M T_s(L-1)/2} \right] \tag{13}$$

The least squares solution [35] to this problem is defined as:

$$\mathbf{w} = \min_{\mathbf{w}} \left|\left| \mathbf{w^T}\mathbf{A} - \mathbf{f_d} \right|\right|_2^2 \tag{14}$$

The minimum norm solution to Equation (14) is given by:

$$\mathbf{w} = \left(\mathbf{A}\mathbf{A^H} \right)^{-1} \mathbf{A}\mathbf{f_d^H} \tag{15}$$

However, if $\mathbf{A}$ is ill-conditioned, the solution will have a large norm, which could amplify signals from outside the required synthetic focus and so a penalised least squares solution is used instead [35]:

$$\min_{\mathbf{w}} \left|\left| \mathbf{w^T}\mathbf{A} - \mathbf{f_d} \right|\right|_2^2 + \lambda \left|\left| \mathbf{w} \right|\right|_2^2 \tag{16}$$

Solving (16) for $\mathbf{w}$ yields the following:

$$\mathbf{w} = \left(\mathbf{A}\mathbf{A^H} - \lambda\mathbf{I} \right)^{-1} \mathbf{A}\mathbf{f_d^H} \tag{17}$$

where $\mathbf{A^H}$ is the Hermitian transpose of $\mathbf{A}$. Assuming the tumour is a point scatterer, the backscattered signal after beamforming will be a distorted time-shifted version of the transmitted pulse, and therefore the size and shape of the backscatterer can be estimated. Since the time delay $\max(T_{rt})$ has already been removed from the signal, the window containing the backscattered response is defined as:

$$ h(r_0, n) = \left\{ \begin{array}{ll} 1, & 0 \leq n \leq n_h \\ 0, & \text{otherwise} \end{array} \right. $$

The energy at the point of interest, r_0, is calculated as the sum of the squares of samples within this window. As described by Bond et al. [20], if the tumour is large, the duration of the backscattered tumour response will be greater, and so a larger window would be more appropriate in this case. However, since we are concerned with the detection of small tumours, a smaller temporal window is chosen to more effectively determine the presence of early-stage cancers. While this may lessen somewhat the strength of the return from larger tumours compared to background clutter, these large tumours inherently provide a much stronger response and so detection of these tumours should not be problematic. The synthetic focus is then scanned throughout the breast in increments of $1\,\text{mm}^2$ (depth and span). The energy is converted to an appropriate pixel intensity with high intensity regions in the image suggesting the possible presence of malignant tissue within the breast.

3. TESTING PROCEDURE AND RESULTS

3.1. FDTD Models

In order to evaluate the Multistatic MIST beamforming algorithm, three Finite Difference Time Domain (FDTD) models, reflecting increasing levels of fibroglandular tissue within the breast are created. These models accurately represent the dielectric properties of the constituent tissues and the highly correlated distribution of these tissues within the breasts [36], and have previously been used by the authors to investigate the effects of dielectric heterogeneity on data-independent beamforming algorithms [37].

The models are that of a naturally flattened breast with the patient lying in the supine position. Therefore, in two dimensions, a sagittal slice of breast is considered with a conformal antenna array placed close to the skin. The adipose/fibroglandular tissue distribution within the breast is established by linearly mapping the regions of adipose and fibroglandular tissue from a high resolution T_2 weighted MR image to the FDTD grid, as previously used by Li [16], Bond [20]

and O'Halloran et al. [37]. The lighter regions within the breast represented fibroglandular tissue, while the darker regions represented adipose tissue. A simple thresholding algorithm was applied to the MRI scan to differentiate between the different regions of tissue, and then a linear transformation algorithm was used to map the tissue distribution in the MRI scan to the FDTD grid. This method was chosen since it preserved the highly correlated nature of fibroglandular tissue distribution in the breast, as opposed to the other methods that model the variance of dielectric properties as being randomly distributed. The antenna array consists of 14 elements modeled as electric-current sources, with the elements equally spaced on the surface of the skin along the horizontal span-axis from 1 cm to 9 cm. The antenna array is backed by a synthetic material matching the dielectric properties of skin.

The first of the three FDTD models is homogeneous and is composed entirely of adipose tissue. This model acts as an "ideal" imaging scenario for the beamformers and is a useful benchmark in determining the effects of dielectric heterogeneity within the breast.

(a) Homogeneous Model   (b) Heterogeneous Model

(b) Dense Model
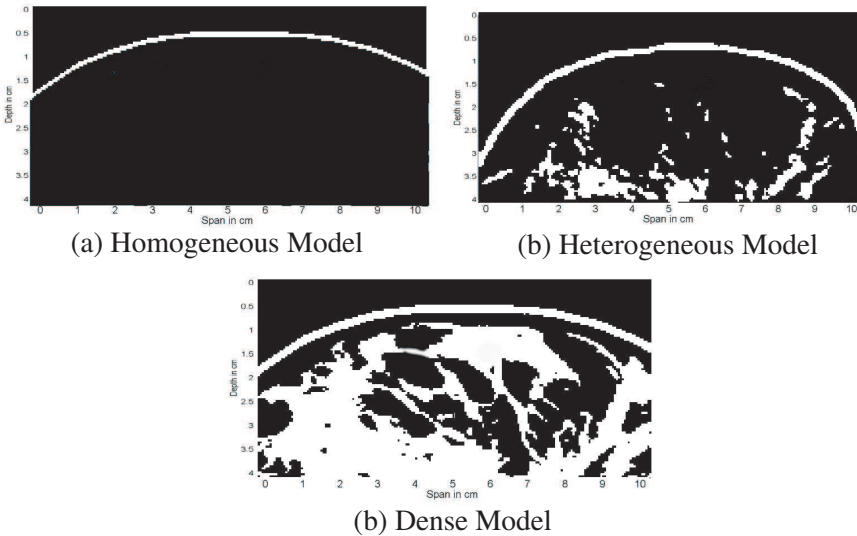
Figure 2. FDTD Models of the breast. The first model is composed entirely of adipose tissue (no fibroglandular tissue), the second heterogeneous model contains a both adipose and fibroglandular tissue and the third model is that of a dense breast where the fibroglandular tissue content is significant. Note: depth is measured on the vertical axis and span is measured on the horizontal axis.

Table 1. Debye parameters for the FDTD model and dielectric properties of each tissue at the centre frequency of the input pulse.

Tissue	ϵ_r	χ_1	σ	t_0 (ps)	Relative Perm.	Cond. (S/m)
Skin	15.63	8.2	0.82	12.6	21.65	2.35
Tumor	7	47	0.15	7	49.2	6.1
Adipose	3.20	1.65	0.035	16	4.30	0.38
Fibroglandular	11.2	38	0.738	12	39.65	7.65

The second model is a heterogeneous model based on an MRI slice taken at a distance from the areola and nipple, where the fibroglandular distribution is less significant. In this model, there are significant regions of fibroglandular tissue, but also regions of adipose tissue where no fibroglandular tissue is present. The third model is a dense model based on a sagittal slice close to the areola, where the fibroglandular tissue distribution is much more significant and presents a much more difficult imaging scenario. The three models are shown in Figure 2, and are referred to as the Homogenous, Heterogenous and Dense models in the remainder of the paper.

The dielectric properties of adipose and fibroglandular tissue used in the FDTD models are based on Lazebnik et al.'s recent studies [32, 33]. The frequency dependence of the dielectric properties were incorporated using Debye models [38]). The Debye parameters for skin are chosen to fit published data by Gabriel et al. [39, 40], while the Debye parameters for malignant tissue are those used by Bond et al. [20]. The Debye parameters for each type of tissue, along with the permittivity and conductivity at the centre frequency, are shown in Table 1.

The FDTD grid resolution, dx, is 0.5 mm and the time step dt is defined as 0.833 ps ($dt = \frac{dx}{2c}$). A specific location within the FDTD model is defined as follows: ($depth$ cm, $span$ cm). A scan involves sequentially illuminating the breast model with a UWB pulse from each antenna, while recording the backscattered signal at all antennas. Since there are 14 antenna array elements, this results in 196 recorded multistatic signals. Before further processing, the signals are downsampled from 1200 GHz (the time step in the FDTD simulation) to 50 GHz. The input signal is a 150-ps differentiated Gaussian pulse, with a centre frequency of 7.5 GHz and a −3 dB bandwidth of 9 GHz.

An idealized artifact removal algorithm, as previously described by Bond [20] and O'Halloran et al. [37] is used to remove the input signal and the reflection from the skin-breast interface. The artifact to

be removed is established by measuring the backscattered signals from the first homogeneous FDTD model with no tumour present. These signals are then subtracted channel-by-channel from the with-tumour responses. Finally, since the input signal is a differentiated Gaussian pulse with a zero crossing at its centre point, the backscattered signal from any dielectric scatterer would also have a zero crossing at its centre point. In order to overcome this, the signals are integrated to produce a maximum at the centre point.

3.2. Metrics

In order to evaluate the robustness and performance of the beamformer, a several different metrics are used:

- Signal-to-Mean Ratio (SMR) [41].
- Signal-to-Clutter Ratio within-breast (SCR) [12, 42, 43].
- The difference between the actual location of the tumor and the location of the peak in the resulting image of backscattered energy (M_{diff}) [31, 43].

The SMR compares the maximum tumor response with the mean response of the different tissues across the breast in the same image of backscattered energy [41]. The SCR within-breast compares the maximum tumor response to the maximum clutter response in the same image. To obtain the value of the maximum clutter, the maximum pixel value of the image is found, excluding the area which includes the tumor peak response up to twice the extent of the Full Width Half Maximum (FWHM) response of the tumor itself [12, 42, 43]. M_{diff} determines the ability of the beamformer to effectively localise the tumor within the breast.

3.3. Results

3.3.1. Effects of Multistatic Channels

The Multistatic MIST beamformer presented in this paper extends the *monostatic* MIST beamformer developed by Bond et al. Therefore, its important to examine the effect of these extra multistatic channels have on the resultant images. Six simulations were completed, with a 10 mm diameter tumor placed at three different locations in both the homogeneous and heterogeneous breast models. The location of the tumors were (1.5 cm, 3.0 cm), (1.5 cm, 5.0 cm) and (1.5 cm, 7.0 cm), with each location defined in terms of (depth cm, span cm). A simple monostatic image using only signals of the form $b_{i,i}[n]$ was created initially, and signals of the form $b_{i,i\pm k}[n]$ were added incrementally. In

this way, the effect of the extra multistatic signals on the algorithms performance (in terms of SCR and SMR) could be determined, and hence the optimum number of multistatic channels could be established empirically. The results of this experiment are shown graphically in Figure 3.

In the homogeneous model, the Multistatic MIST beamformer outperformed the monostatic MIST beamformer by 2–3 dB and 2.5–5 dB in terms of SMR and SCR respectively. Similarly, in the heterogeneous model, the Multistatic beamformer also showed an improved performance of 2–6 dB and 2–7 dB in terms of SMR and SCR, as shown in Figure 3. Figures 4(a) and (b) show the resultant images created by the monostatic and Multistatic MIST beamformers
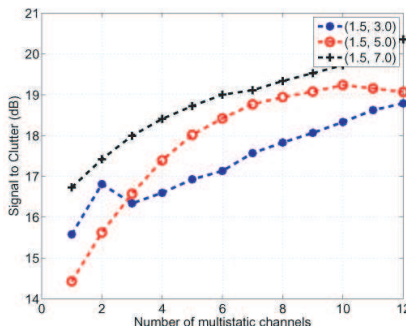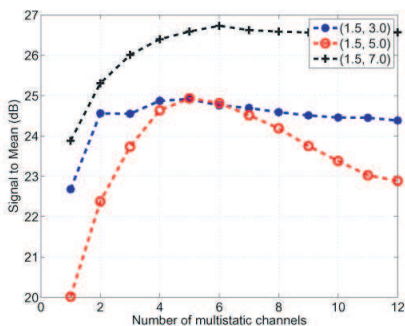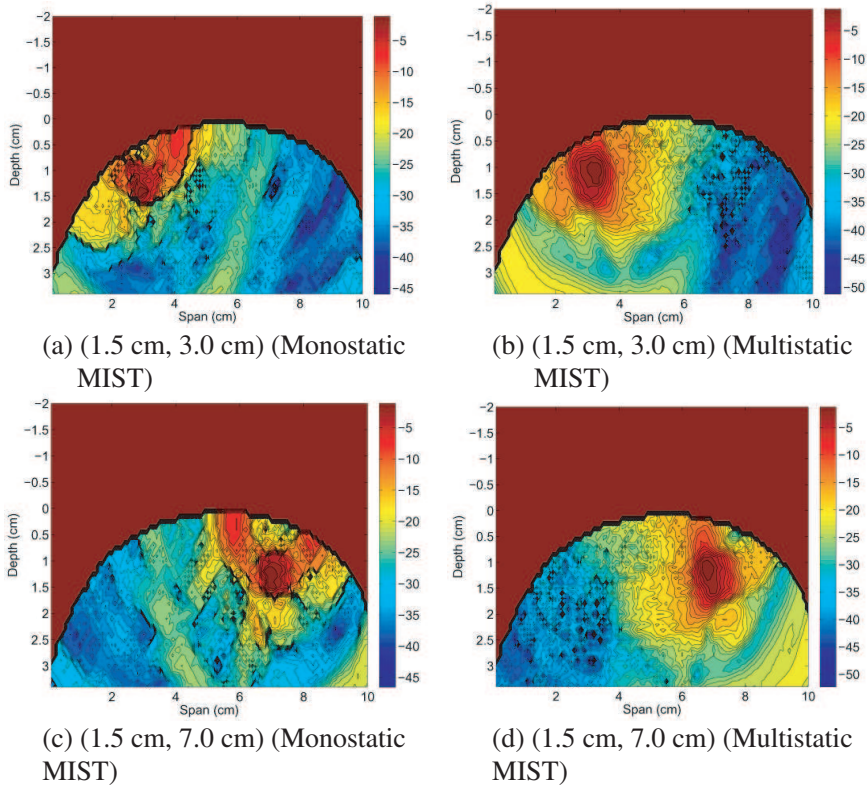
(a) Signal To Mean (Homogeneous Model)

(b) Signal To Clutter (Homogeneous Model)
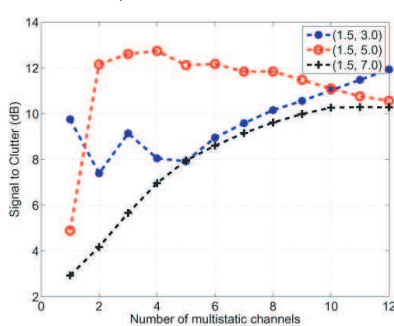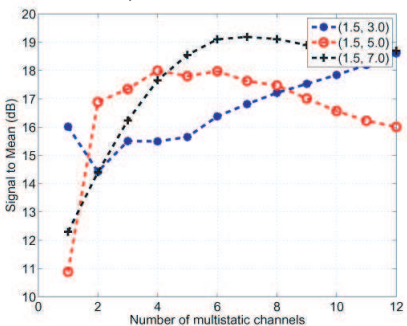
(c) Signal To Mean (Heterogeneous Model)

(d) Signal To Clutter (Heterogeneous Model)

Figure 3. The effect of multistatic channels on the performance of the MIST beamformer. The SMR and SCR ratio for homogeneous and heterogeneous breast models are shown in shown in Figures (a) and (b), and (c) and (d) respectively.

(a) (1.5 cm, 3.0 cm) (Monostatic MIST)

(b) (1.5 cm, 3.0 cm) (Multistatic MIST)

(c) (1.5 cm, 7.0 cm) (Monostatic MIST)

(d) (1.5 cm, 7.0 cm) (Multistatic MIST)

Figure 4. Comparison of images created by the monostatic and multistatic MIST beamformer. Figures (a) and (b) show images created by the monostatic and multistatic MIST beamformer respectively of a tumour located at (1.5 cm, 3.0 cm). A similar comparison is shown in Figures (c) and (d) with a tumor at location (1.5 cm, 7.0 cm).

respectively of a tumor located at (1.5 cm, 3.0 cm), while Figures 4(c) and (d) show corresponding images for a tumor located at (1.5 cm, 7.0 cm). The images are shown side-by-side for direct comparison. In both cases, the presence and precise location of the tumor is much more clearly identifiable in the Multistatic MIST image.

3.3.2. Lateral and Depth Localisation

An important attribute of any breast imaging modality is the ability to precisely determine the location of any tumor tissue within the breast. In order to evaluate the lateral localisation ability of the beamformer, 5 FDTD simulations were performed with a tumor positioned at 5 different locations 1 cm apart, and at a constant depth of 1.5 cm. All

tests were performed in the homogeneous distribution model. The distance between the actual location of the tumor and the peak tumor response in the resultant image is calculated for each simulation and is presented in Table 2. The average error was found to be approximately 5.9 mm.

Similarly, the depth localisation ability of the beamformer was examined by completing 5 simulations where the lateral location of the tumour was constant, and the depth of the tumour was varied. Once again the distance between the actual tumour location and the location of the peak tumour response in the resultant images was recorded. The results are shown in Table 3. The average error in the depth localisation was found to be approximately 5.6 mm. In all tests, the peak of the tumour response occurred 5 to 6 mm shallower than the actual centre of the tumour. This localization error is due to the fact that the tumour was 1 cm in diameter and therefore the surface of the tumour closest to the antenna array was at a distance of 5 mm from the tumour centre; the reflection from the tumour is generated at the surface of the tumour. The localisation ability of the beamformer could potentially be improved by using a cylindrical rather than a planar antenna configuration [43].

Table 2. Evaluation of the lateral localization ability of the multistatic MIST beamformer.

| Sim. No.	Actual Tumour Location	Location in Image	Error (mm)
1	(1.5 cm, 3.0 cm)	(1.0 cm, 3.3 cm)	5.83
2	(1.5 cm, 4.0 cm)	(0.9 cm, 4.2 cm)	6.32
3	(1.5 cm, 5.0 cm)	(0.9 cm, 4.9 cm)	6.08
4	(1.5 cm, 6.0 cm)	(0.9 cm, 5.8 cm)	6.32
5	(1.5 cm, 7.0 cm)	(1.0 cm, 6.8 cm)	5.38

Table 3. Evaluation of the depth localization ability of the multistatic MIST beamformer.

| Sim. No.	Actual Tumour Location	Location in Image	Error (mm)
1	(1.5 cm, 5.0 cm)	(0.9 cm, 4.9 cm)	6.08
2	(2.0 cm, 5.0 cm)	(1.4 cm, 4.9 cm)	6.08
3	(2.5 cm, 5.0 cm)	(2.0 cm, 5.0 cm)	5.0
4	(3.0 cm, 5.0 cm)	(2.6 cm, 5.0 cm)	4.0
5	(3.5 cm, 5.0 cm)	(3.0 cm, 5.0 cm)	5.0

3.3.3. Robustness to Tumor Size

Early detection and intervention is key to the successful treatment of breast cancer [2]. Therefore, the ability of the UWB imaging technology to detect tumours $\leq 10\,\text{mm}$ is critical to its application as an effective imaging alternative to traditional X-ray mammography. Four test scenarios are considered: A 12 mm, 10 mm, 7.5 mm and 5 mm tumour positioned at location (1.5 cm, 3.0 cm). The tests are repeated across the homogeneous and heterogeneous models and the SCR and SMR ratios are recorded. The results are shown in Figure 5.
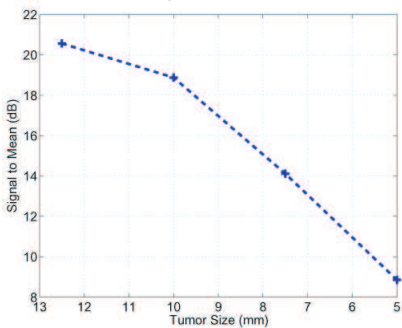
Both the SMR and SCR decrease significantly with decreasing tumor size. However, even for the smallest tumor (5 mm in diameter), there still exists a significant contrast between the tumor and the background clutter, with a SMR of 9 dB and a SCR of 3 dB across both distributions.
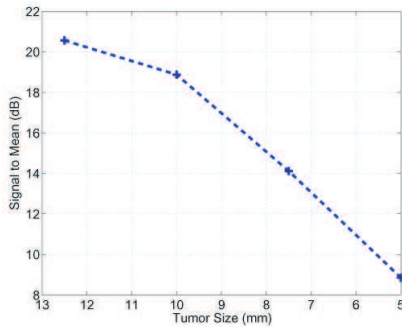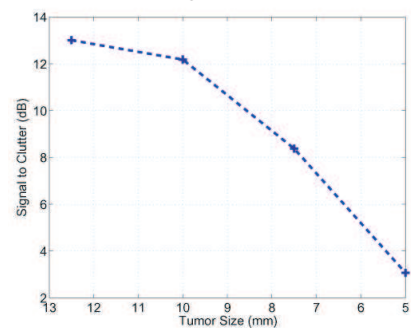

(a) SMR Versus Tumor Size
(Homogeneous Model)
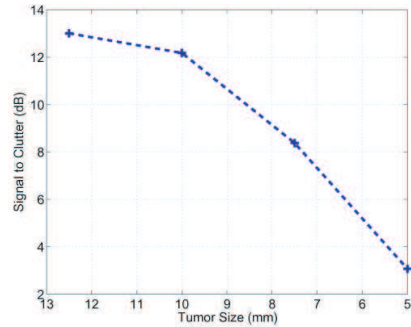
(b) SCR Versus Tumor Size
(Homogeneous Model)

(c) SMR Versus Tumor Size
(Heterogeneous Model)

(d) SCR Versus Tumor Size
(Heterogeneous Model)

Figure 5. Variation of SMR and SCR ratios with tumor size for the homogeneous, Figures 5(a) and 5(b), and heterogeneous models, Figures 5(c) and 5(d).

In all imaging scenarios examined up to this point, the assumed average dielectric properties of the breast used by the beamformer precisely matched the actual average dielectric properties of the numerical breast phantom. In the next section, the robustness of the beamformer to incorrectly assumed dielectric properties is evaluated.

3.3.4. Natural Variations in Dielectric Properties

The dielectric properties of normal breast tissue has been shown to vary significantly between patients [32, 44]. Recently, Lazebnik et al. established three groups of normal tissue, based on the low, medium and high percentile dielectric properties for normal adipose and fibroglandular tissue [32]. For completeness, it is appropriate to examine the effectiveness of the beamformer in detecting tumors in each type of normal breast tissue. Three FDTD breast models are created based on the low, medium and high percentile dielectric properties, and the heterogeneous distribution model. A 10 mm tumor is placed at two different locations within each model, (1.5 cm, 3.0 cm) and (1.5 cm, 7.0 cm). Once again, the SMR and SCR performance metrics are calculated for each simulation.

The SCR and SMR is greatest in the low percentile breast model, where there exists a greater dielectric contrast between the normal and malignant breast tissue.

### 3.3.5. Fibroglandular Distribution

In order to examine the robustness of the beamformer to fibroglandular tissue dsitribution, a homogeneous, heterogeneous and dense breast model were created as described previously. A 10 mm diameter tumor was positioned at three different locations, (1.5 cm, 3.0 cm), (1.5 cm, 5.0 cm) and (1.5 cm, 7.0 cm), in each of the three models. The backscattered signals were recorded and an image of each breast was created using the Multistatic MIST beamformer. The SMR and SCR, plotted as a function of fibroglandular tissue distribution, are shown in Figure 7. Both the SMR and SCR decrease considerably with increased fibroglandular tissue content. There are three specific reasons for this decrease:

- As the breast becomes more dielectrically heterogeneous, there is a reduced dielectric contrast between normal and cancerous breast tissue.
- The increased fibroglandular content in the more dense breast means constructive addition of UWB backscattered signals is much more difficult.

• The MIST beamformer assumes that the breast is primarily dielectrically homogeneous, and therefore cannot appropriately compensate for the attenuation and phase distortion as the UWB signals propagate through the fibroglandular tissue.
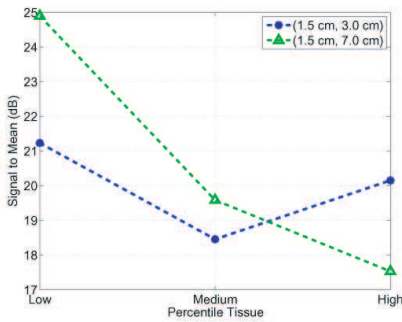

(a) SMR Versus Natural Variation in Dielectric Properties
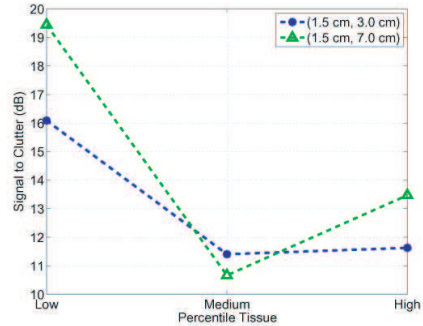
(b) SCR Versus Natural Variation in Dielectric Properties

Figure 6. Effects of natural variations in the dielectric properties of normal breast tissue on the performance of the Multistatic MIST beamformer. Two tumor positioned are considered in three breast models based on the low, medium and high percentile dielectric properties established by Lazebnik et al.. SMR Versus dielectric heterogeneity is shown in (a), while SCR versus dielectric heterogeneity is shown in (b).
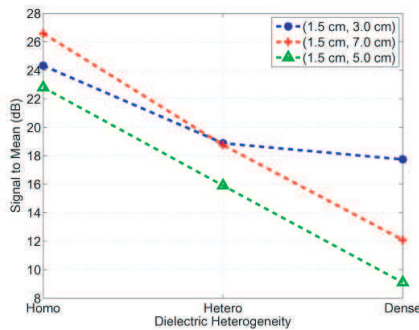
(a) SMR Versus Dielectric Heterogeneity
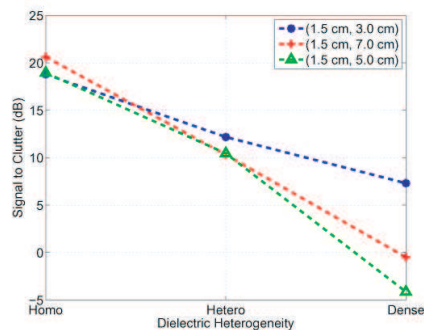
(b) SCR Versus Dielectric Heterogeneity

Figure 7. Effects of dielectric heterogeneity on the performance of the Multistatic MIST beamformer. Three tumor positioned are considered in three breast models with increasing fibroglandular tissue content. The SMR and SCR both decrease significantly with increasing fibroglandular content.

4. CONCLUSIONS

This paper has examined the performance and robustness of a multistatic MIST beamformer, previously proposed by the authors. The multistatic beamformer improves on the performance of the monostatic beamformer by exploiting the additional information from multiple receive antennas.The beamformed multistatic channels have been shown to add coherently at the site of significantly dielectric scatterers, and provide a considerable improvement in terms of both SMR and SCR in the resultant images compared to the monostatic MIST beamformer. The robustness of the Multistatic beamformer to the range of dielectric properties of normal breast tissue and different fibroglandular tissue distributions has also been investigated. Three 2D numerical breast models, based on a homogeneous, heterogeneous and dense distribution of fibroglandular tissue have been developed to comprehensively evaluate the performance of the beamformer. Tumours as small as 5 mm have been successfully imaged using the Multistatic beamformer. However, while the beamformer performs well in the homogeneous and heterogeneous distributions, the presence and exact location of a tumour in the dense model is much more difficult to establish. This is due in part to the large difference between the assumed homogeneous channel model and the actual heterogeneous channel, and is a problem shared by all data-independent beamformers [37]. Methods to better estimate the overall average dielectric properties of patient specific breast tissue, such as those developed by Winters et al. [45, 46], could be incorporated into future beamforming algorithms. Future work will involve extension of the numerical breast phantom to 3 dimensions, the investigation of classification techniques to differentiate between normal, benign and malignant tissue, and methods to estimate the patient-specific dielectric properties of the breast.

ACKNOWLEDGMENT

REFERENCES

1. Society, A. C., "Cancer facts and figures 2008," American Cancer Society, 2008.

2. Nass, S. L., I. C. Henderson, and J. C. Lashof, *Mammography*

   and Beyond: Developing Technologies for the Early Detection of Breast Cancer, National Academy Press, 2001.

3. Bulyshev, A. E., S. Y. Semenov, A. E. Souvorov, R. H. Svenson, A. G. Nazorov, Y. E. Sizov, and G. P. Tatsis, "Computational modeling of three-dimensional microwave tomography of breast cancer," *IEEE Trans. Biomed. Eng.*, Vol. 48, No. 9, 1053–1056, Sep. 2001.

4. Meaney, P. M., M. W. Fanning, D. Li, S. P. Poplack, and K. D. Paulsen, "A clinical prototype for active microwave imaging of the breast," *IEEE Trans. Microwave Theory Tech.*, Vol. 48, No. 11, 1841–1853, Nov. 2000.

5. Meaney, P. M., K. D. Paulsen, J. T. Chang, M. W. Fanning, and A. Hartov, "Nonactive antenna compensation for fixed-array microwave imaging: Part II — Imaging results," *IEEE Trans. Med. Imag.*, Vol. 18, No. 6, 508–518, Jun. 1999.

6. Souvorov, A. E., A. E. Bulyshev, S. Y. Semenov, R. H. Svenson, and G. P. Tatis, "Two-dimensional analysis of a microwave flat antenna array for breast cancer tomography," *IEEE Trans. Microwave Theory Tech.*, Vol. 48, No. 8, 1413–1415, Aug. 2000.

7. Liu, Q. H., Z. Q. Zhang, T. Wang, J. A. Byran, G. A. Ybarra, L. W. Nolte, and W. T. Joines, "Active microwave imaging I - 2-D forward and inverse scattering methods," *IEEE Trans. Microwave Theory Tech.*, Vol. 50, No. 1, 123–133, Jan. 2002.

8. Yu, C., M. Yuan, J. Stang, E. Bresslour, R. T. George, G. A. Ybarra, and W. Joines, "Active microwave imaging II: 3-D system prototype and image reconstruction from experimental data," *IEEE Trans. Microwave Theory Tech.*, Vol. 56, No. 4, 991–1000, 2008.

9. Meaney, P. M., M. W. Fanning, T. Raynolds, C. J. Fox, Q. Fang, C. A. Kogel, S. P. Poplack, and K. D. Paulsen, "Initial clinical experience with microwave breast imaging in women with normal mammography," *Academic Radiology*, Vol. 14, No. 2, 207–218, 2007.

10. Hagness, S. C., A. Taflove, and J. E. Bridges, "Two-dimensional FDTD analysis of a pulsed microwave confocal system for breast cancer detection: Fixed-focus and antenna-array sensors," *IEEE Trans. Biomed. Eng.*, Vol. 45, No. 12, 1470–1479, 1998.

11. Susan, C., A. Taflove, and J. E. Bridges, "Three-dimensional FDTD analysis of a pulsed microwave confocal system for breast cancer detection: Design of an antennaarray element," *IEEE Trans. Antennas and Propagat.*, Vol. 47, No. 5, 783–791, May 1999.

12. Fear, E. C., X. Li, S. C. Hagness, and M. A. Stuchly, "Confocal microwave imaging for breast cancer detection: Localization of tumors in three dimensions," *IEEE Trans. Biomed. Eng.*, Vol. 49, No. 8, 812–822, Aug. 2002.

13. Fear, E. C. and M. A. Stuchly, "Microwave system for breast tumor detection," *IEEE Microwave and Guided Wave Letters*, Vol. 9, No. 11, 470–472, Nov. 1999.

14. Fear, E. C., J. Sill, and M. A. Stuchly, "Experimental feasibility study of confocal microwave imaging for breast tumor detection," *IEEE Trans. Microwave Theory Tech.*, Vol. 51, No. 3, 887–892, Mar. 2003.

15. Fear, E. C., J. Sill, and M. A. Stuchly, "Experimental feasibility study of confocal microwave imaging for breast tumor detection," *IEEE Trans. Microwave Theory Tech.*, Vol. 51, No. 3, 887–892, Mar. 2003.

16. Li, X. and S. C. Hagness, "A confocal microwave imaging algorithm for breast cancer detection," *IEEE Microwave and Wireless Components Letters*, Vol. 11, No. 3, 130–132, 2001.

17. Li, X., E. J. Bond, B. D. V. Veen, and S. C. Hagness, "An overview of ultra-wideband microwave imaging via space-time beamforming for early-stage breast-cancer detection," *IEEE Antennas and Propagation Magazine*, Vol. 47, No. 1, 19–34, Feb. 2005.

18. Craddock, I. J., R. Nilavalan, J. Leendertz, A. Preece, and R. Benjamin, "Experimental investigation of real aperture synthetically organised radar for breast cancer detection," *IEEE AP-S International Symposium*, Washington, DC, 2005.

19. Hernandez-Lopez, M., M. Quintillan-Gonzalez, S. Garcia, A. Bretones, and R. Martin, "A rotating array of antennas for confocal microwave breast imaging," *Microw. Opt. Technol. Lett.*, Vol. 39, No. 4, 307–311, Nov. 2003.

20. Bond, E. J., X. Li, S. C. Hagness, and B. D. V. Veen, "Microwave imaging via space-time beamforming for early detection of breast cancer," *IEEE Trans. Antennas and Propagat.*, No. 8, 1690–1705, Aug. 2003.

21. Davis, S. K., E. J. Bond, X. Li, S. C. Hagness, and B. D. van-Veen, "Microwave imaging via space-time beamforming for the early detection of breast cancer: Beamformer design in the frequency domain," *Journal of Electromagnetic Waves and Applications*, Vol. 17, No. 2, 357–381, 2003.

22. Li, X., S. K. Davis, S. C. Hagness, D. W. van der Weide, and B. van Veen, "Microwave imaging via space-time beamforming: Experimental investigation of tumor detection in multilayer breast

phantoms," *IEEE Trans. Microwave Theory Tech.*, Vol. 52, No. 2, 1856–1865, Aug. 2002.

23. Li, X., E. J. Bond, S. C. Hagness, B. D. V. Veen, and D. van der Weide, "Three-dimensional microwave imaging via space-time beamforming for breast cancer detection," *IEEE AP-S International Symposium and USNC/USRI Radio Science Meeting*, San Antonio, TX, USA, Jun. 2002.

24. Xie, Y., B. Guo, L. Xu, J. Li, and P. Stoica, "Multistatic adaptive microwave imaging for early breast cancer detection," *IEEE Trans. Biomed. Eng.*, Vol. 53, No. 8, 1647–1657, Aug. 2006.

25. Xie, Y., B. Guo, J. Li, and P. Stoica, "Novel multistatic adaptive microwave imaging methods for early breast cancer detection," *EURASIP J. Appl. Si. P.*, Vol. 2006, No. 91961, 1–13, 2006.

26. Gao, B., Y. Wang, J. Li, P. Stoica, and R. Wu, "Microwave imaging via adaptive beamforming methods for breast cancer detection," *PIERS Online*, Vol. 1, No. 3, 350–353, 2005.

27. Craddock, I. J., R. Nilavalan, A. Preece, and R. Benjamin, "Experimental investigation of real aperture synthetically organised radar for breast cancer detection," *IEEE Antennas and Propagation Society International Symposium*, Vol. 1B, 179–182, Washington, DC, 2005.

28. Klemm, M., I. J. Craddock, J. A. Leendertz, A. W. Preece, and R. Benjamin, "Radar-based breast cancer detection using a hemispherical antenna array-experimental results," *IEEE Trans. Antennas and Propagat.*, Vol. 57, No. 6, 1692–1704, 2009.

29. Nilavalan, R., A. Gbedemah, X. Li, and S. C. Hagness, "Numerical investigation of breast tumour detection using multi-static radar," *IET Electronic Letters*, Vol. 39, No. 25, 1787–1789, Dec. 2003.

30. Guo, B., Y. Wang, J. Li, P. Stoica, and R. Wu, "Microwave imaging via adaptive beamforming methods for breast cancer detection," *PIERS Online*, Vol. 1, No. 3, 350-353, 2005.

31. O'Halloran, M., M. Glavin, and E. Jones, "Quasi-multistatic MIST beamforming for the early detection of breast cancer," *IEEE Trans. Biomed. Eng.*, in Press.

32. Lazebnik, M., L. McCartney, D. Popovic, C. B. Watkins, M. J. Lindstrom, J. Harter, S. Sewall, A. Magliocco, J. H. Booske, M. Okoniewski, and S. C. Hagness, "A large-scale study of the ultrawideband microwave dielectric properties of normal breast tissue obtained from reduction surgeries," *Phys. Med. Biol.*, Vol. 52, 2637–2656, 2007.

33. Lazebnik, M., D. Popovic, L. McCartney, C. B. Watkins,

M. J. Lindstrom, J. Harter, S. Sewall, T. Ogilvie, A. Magliocco, T. M. Breslin, W. Temple, D. Mew, J. H. Booske, M. Okoniewski, and S. C. Hagness, "A large-scale study of the ultrawideband microwave dielectric properties of normal, benign and malignant breast tissues obtained from cancer surgeries," *Phys. Med. Biol.*, Vol. 52, 6093–6115, 2007.

34. Sha, L., E. R. Ward, and B. Stroy, "A review of the dielectric properties of normal and malignant breast tissue," *Proceedings of the IEEE SoutheastCon*, Columbia, South Carolina, USA, Apr. 2002.

35. Haykin, S., *Adaptive Filter Theory*, 4th edition, Prentice Hall, 2001.

36. O'Halloran, M., R. Conceicao, D. Byrne, M. Glavin, and E. Jones, "FDTD modeling of the breast: A review," *Progress In Electromagnetics Research B*, Vol. 18, 1–24, 2009.

37. O'Halloran, M., M. Glavin, and E. Jones, "Effects of fibroglandular tissue distribution on data-independent beamforming algorithms," *Progress In Electromagnetics Research*, Vol. 97, 141–158, 2009.

38. Lazebnik, M., M. Okoniewski, J. Booske, and S. Hagness, "Highly accurate debye models for normal and malignant breast tissue dielectric properties at microwave frequencies," *Microwave and Wireless Components Letters, IEEE*, Vol. 17, No. 12, 822–824, Dec. 2007.

39. Gabriel, C., S. Gabriel, and E. Corthout, "The dielectric properties of biological tissues: I. Literature survey," *Phys. Med. Biol.*, Vol. 41, 2231–2249, 1996.

40. Gabriel, S., R. W. Lau, and C. Gabriel, "The dielectric properties of biological tissues: II. Measurements in the frequency range 10 Hz to 20 GHz," *Phys. Med. Biol.*, Vol. 41, 2251–2269, 1996.

41. Lim, H. B., N. T. T. Nhung, E. P. Li, and N. D. Thang, "Confocal microwave imaging for breast cancer detection: Delay-multiplyand-sum image reconstruction algorithm," *IEEE Trans. Biomed. Eng.*, Vol. 55, No. 6, 1697–1704, Jun. 2008.

42. Fear, E. C. and M. Okoniewski, "Confocal microwave imaging for breast tumor detection: Application to a hemispherical breast model," *2002 IEEE MTT-S International Microwave Symposium Digest*, Vol. 3, 1759–1762, Seattle, WA, USA, 2002.

43. Conceição, R. C., M. O'Halloran, M. Glavin, and E. Jones, "Antenna configurations for ultra wide band radar detection of breast cancer," *SPIE BIOS West*, Vol. 7169, San Jose, CA, Jan. 2009.

44. Campbell, A. M. and D. V. Land, "Dielectric properties of female human breast tissue measured in vitro at 3.2 GHz," *Phys. Med. Biol.*, Vol. 37, No. 1, 193–210, 1992.

45. Winters, D. W., E. J. Bond, S. C. Hagness, and B. D. van Veen, "Estimation of the average breast tissue properties at microwave frequencies using a time-domain inverse scattering technique," *Proc. EMC*, 59–64, Zurich, Feb. 2005.

46. Winters, D. W., E. J. Bond, and S. C. Hagness, "Estimation of the frequency-dependent average dielectric properties of breast tissue using a time-domain inverse scattering technique," *IEEE Trans. Antennas and Propagat.*, Vol. 55, 3517–3528, 2006.